Machine Design

Critical Engine Speed in an Engine Connecting Rod

Project Report

Lorenzo Dalla Rosa



Project Report

SUPERVISORS
Prof. Francesco Frendo
Prof. Andrea Chiocca

Academic Year 2025/2026

Contents

1 Introduction **1**
1.1 Engineering Problem 1
1.2 Analytical Model 2

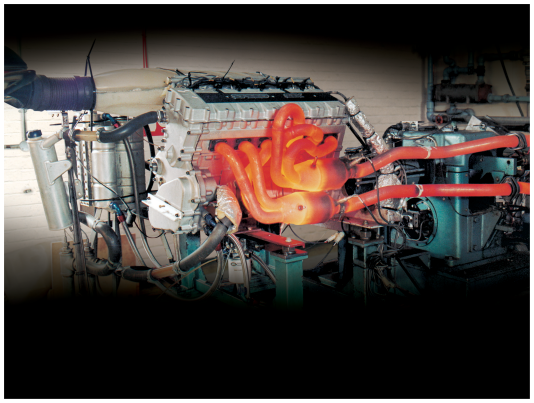
2 FEM Model **4**
2.1 CAD Model 4
2.2 Real System and Geometric Simplifications 4
2.3 Material Properties and Mesh 4
2.4 Loads and Boundary Conditions 5
2.5 Contacts 5

3 Results **6**
3.1 Finite Element Results 6

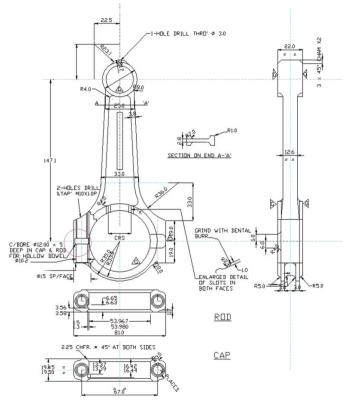
4 Discussion of Results **8**
4.1 Comparison with Theoretical or Empirical Predictions 8
4.2 Influence of Modelling Assumptions 8
4.3 Mesh Independence Study 9
4.4 Model Limitations and Possible Improvements 9

1 Introduction

The original 3.5-litre TVR AJP6 was a straight-six, 24-valve engine designed by Al Melling in the mid-1990s and subsequently developed into the production Speed Six. The later T350 used a 3605 cm^3 version rated at a maximum of 350 hp. This engine was selected because it is one of the few high-performance engines for which original technical blueprints are publicly available, enabling the connecting rod to be reconstructed from original design data.



(a) TVR AJP6/Speed Six engine undergoing dynamometer testing.



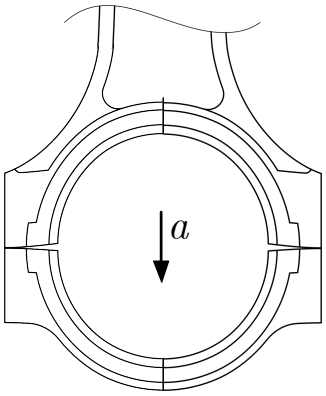
(b) Original technical drawing of the 3.5-litre connecting rod and big-end cap.

Parameter	Specification
Bore	3.780 in
Stroke	3.170 in
Number of cylinders	6
Cylinder volume	582.95 cm^3
Connecting-rod length	147.1 mm

1.1 Engineering Problem

The engineering problem is to determine the limiting engine speed N_{crit} at which inertial loading at top dead centre (TDC) initiates separation between the connecting rod and its big-end cap. In this analysis, separation is defined as the existence of at least one point on the mating interface at which the contact pressure falls to zero.

The assembly comprises the connecting-rod body, detachable big-end cap, two M10×1.25×35 class 12.9 screws and two hollow dowel pins. The screws clamp the cap around the crankpin journal, while the dowels align the components and transfer the shear load across the joint.



The material properties are listed in Table 1. Density is required for the inertial loads.

Component and material	ρ (kg/m^3)	E (GPa)	ν	S_y (MPa)	S_u (MPa)
Connecting rod and cap: EN30B/4340 steel	7850	210	0.29	820	1020
Hollow dowel pin: hardened 100Cr6 steel	7810	210	0.29	1200	1400
Fasteners: property class 12.9	7850	205	0.30	1100	1200

Table 1: Material properties of the assembly components.

With no producer-specified tightening procedure available, each screw is preloaded to 75% of the yield load. For an M10×1.25 thread,

$$A_S = \frac{\pi}{4}\,(d - 0.9382p)^2 = 61.2\,\mathrm{mm}^2, \qquad F_i = 0.75 S_y A_S = 50.5\,\mathrm{kN}.$$

The mechanism is modelled as a planar slider–crank system rotating at a constant engine speed N. At TDC, the acceleration of the reciprocating assembly is directed towards the crankshaft and reaches its maximum magnitude. The corresponding inertia force acts away from the crankshaft, placing the rod and its big-end joint in tension and progressively reducing the compressive contact pressure at the rod–cap interface as the engine speed increases.

Given the geometric parameters

$$R = \frac{3.170\,\mathrm{in}}{2} = 40.26\,\mathrm{mm}, \qquad L = 147.1\,\mathrm{mm}, \qquad \lambda = \frac{R}{L} = 0.2737.$$

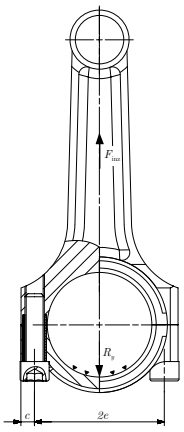
Using the second-order slider–crank approximation, the TDC acceleration for an engine speed N in rpm is

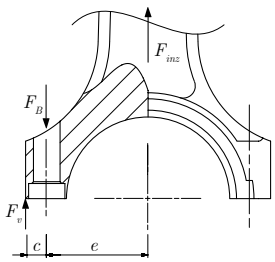
$$a_{\mathrm{TDC}} \simeq -R\left(\frac{2\pi N}{60}\right)^2 (1+\lambda).$$

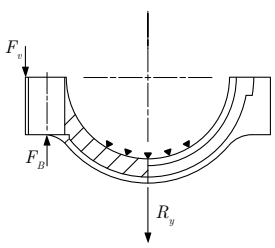
1.2 Analytical Model

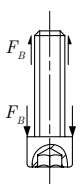
The inertial load is evaluated using an equivalent reciprocating mass comprising the piston assembly and the portion of the connecting rod associated with the small end, $m_{\mathrm{eq}} = 600\,\mathrm{g}$. The inertia of the big-end cap and screws is neglected. The hollow dowel is also omitted because it is fixed in the rod but can slide within the cap, providing negligible resistance to separation, as discussed in Section 4.2. The tensile inertial force acting on the connecting rod at TDC is therefore

$$F_{\mathrm{inr}} = -m_{\mathrm{eq}} a_{\mathrm{TDC}} \simeq m_{\mathrm{eq}} R\left(\frac{2\pi N}{60}\right)^2 (1+\lambda).$$









The external load acting on the bolted joint is amplified by the lever effect. The bolt–fulcrum distance is $c = 7\,\mathrm{mm}$ and the load eccentricity is $e = 33.5\,\mathrm{mm}$, assumed approximately constant during loading. With symmetric load sharing between the two screws,

$$F_e = \frac{F_{\mathrm{inr}}}{2}\left(1 + \frac{e}{c}\right), \qquad F_v = F_{\mathrm{inr}}\frac{e}{c}.$$

The bolted section is too compact for the conventional elastic pressure-cone approximation because the force paths are bounded by the walls of the connecting rod and cap. Assuming parallel force paths, the effective resisting section area is

$$A_{\mathrm{ers}} = A_{\mathrm{sec}} = 119.29\,\mathrm{mm}^2.$$

The stiffness of the clamped section is obtained from

$$\delta_C = \delta_C^{(1)} + \delta_C^{(2)}, \qquad k_C = \delta_C^{-1}, \qquad \delta_C^{(1)} = \frac{L_s - l_{\mathrm{eng}}}{E_C A_{\mathrm{ers}}}, \qquad \delta_C^{(2)} = \frac{\beta d}{E_C A_N}.$$

Here, $L_s = 35\,\mathrm{mm}$, $l_{\mathrm{eng}} = 11\,\mathrm{mm}$, $d = 10\,\mathrm{mm}$, $\beta = 0.33$, $A_N = \pi d^2/4 = 78.54\,\mathrm{mm}^2$ and $E_C = 210\,\mathrm{GPa}$. Therefore,

$$\delta_C = 1.158 \times 10^{-6}\,\mathrm{mm/N}, \qquad k_C = 863\,\mathrm{kN/mm}.$$

The screw stiffness is evaluated by adding the compliance of the unengaged threaded length and the local compliance beneath the head and within the engaged thread. The total screw compliance and stiffness are

$$\delta_B = \delta_B^{(1)} + \delta_B^{(2)} + \delta_B^{(3)}, \qquad k_B = \delta_B^{-1}.$$

The three contributions, written in load-path order, are

$$\delta_B^{(1)} = \frac{L_s - l_{\mathrm{eng}}}{E_B A_S}, \qquad \delta_B^{(2)} = \frac{\beta d}{E_B A_N}, \qquad \delta_B^{(3)} = \frac{\beta d}{E_B A_S}.$$

Here, $A_S = 61.2\,\mathrm{mm}^2$ is the tensile-stress area, $A_N = 78.54\,\mathrm{mm}^2$ is the nominal shank area, $E_B = 205\,\mathrm{GPa}$ and $\beta = 0.33$. Using $L_s = 35\,\mathrm{mm}$, $l_{\mathrm{eng}} = 11\,\mathrm{mm}$ and $d = 10\,\mathrm{mm}$ gives

$$\delta_B = 2.381 \times 10^{-6}\,\mathrm{mm/N}, \qquad k_B = 420\,\mathrm{kN/mm}.$$

The fraction of the external joint load carried by the screw is determined by the relative stiffnesses:

$$\xi = \frac{k_B}{k_B + k_C} = 0.327.$$

The screw force F_B and the residual compressive force in the clamped section F_C are therefore

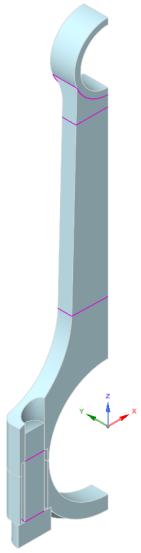
$$\begin{cases} F_B = F_i + \xi F_e, \\ F_C = F_i - (1 - \xi)F_e. \end{cases}$$

The critical condition is reached when the compressive force falls to zero, $F_C = 0$, corresponding to the onset of joint separation. Substituting the expressions for F_e and F_{inr} gives

$$N_{\mathrm{crit}} = \frac{60}{2\pi}\sqrt{\frac{2F_i}{m_{\mathrm{eq}}(1-\xi)\left(1 + \dfrac{e}{c}\right)R(1+\lambda)}} \simeq 8770\,\mathrm{rpm}.$$

2 FEM Model

2.1 CAD Model



The connecting-rod assembly was reconstructed parametrically in **Siemens NX** from the original blueprint. A complete model was then simplified using the **WAVE Geometry Linker** that maintains an associative link between the complete and simplified geometries, so changes to the original model propagate automatically.

The cylindrical-head screws were simplified as two coaxial cylinders representing the head and body. The body diameter was selected so that its cross-sectional area equals the tensile-stress area A_S of the M10×1.25 thread. The dowel pin was represented as a hollow cylinder. All big-end fillets were retained because sharp edges would introduce unrealistic local stress concentrations.

The simplified geometry was imported into **Ansys Workbench** and prepared in **Ansys SpaceClaim**. Since the assembly has two symmetry planes, only one quarter of the complete geometry was required for the FEM analysis, significantly reducing the node count. Additional partitions were introduced to control mesh distribution and element alignment. Shared topology connected the partitioned regions, producing a conformal mesh across their interfaces at substantially lower computational cost than equivalent bonded contact definitions.

2.2 Real System and Geometric Simplifications

The hollow-dowel surface was split to distinguish the portion fixed in the connecting rod from that allowed to slide within the cap. Each screw was divided into engaged and unengaged regions to represent the threaded connection and free screw length separately.

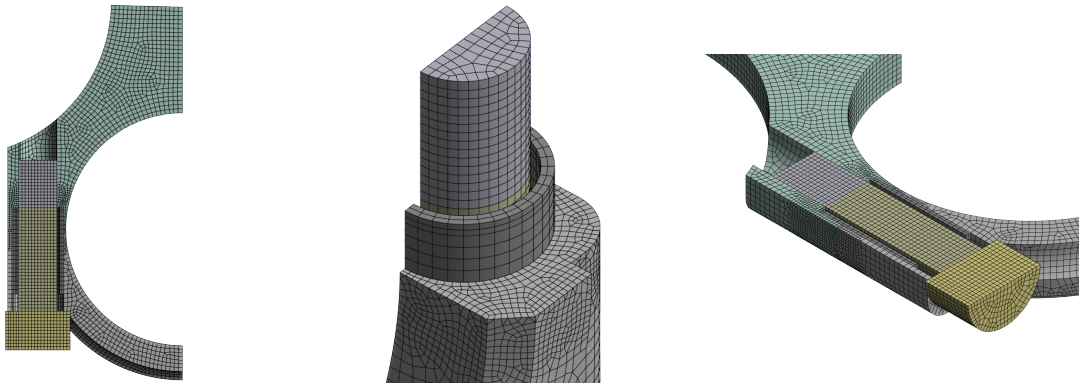
The hydrodynamic crankpin support was simplified by applying a zero remote-displacement condition over a 120° arc on the lower big-end bore. This provides a distributed support without constraining the entire bore and is appropriate for predicting global rod–cap opening, but not local bearing pressure.

The connecting-rod shank was truncated near the big end, and the removed rod portion and piston assembly were replaced by an equivalent point mass coupled to the cut face. This preserves the inertial load transmitted to the joint while reducing the mesh size considerably.

2.3 Material Properties and Mesh

The materials listed in Table 1 were defined in an Ansys Engineering Data block. Each material uses a linear isotropic elasticity model. A Hex Dominant method was enforced for the connecting rod and cap. The geometric partitions introduced in SpaceClaim guide the element distribution and allow a high-quality predominantly hexahedral mesh to be generated in these components. A further local refinement, with an element size of 0.5 mm, was applied to the main rod–cap contact region to resolve the contact-pressure gradient and the onset of separation more accurately. The hollow dowel was meshed using a Sweep method, together with an edge-sizing control that enforces two elements through its wall thickness. This prevents the thin cylindrical wall from being represented by a single element, which could produce artificial stiffness (shear locking). The simplified fastener was meshed using the

MultiZone method to obtain an orderly hexahedral-dominant mesh along its axial regions.



2.4 Loads and Boundary Conditions

A bolt-preload boundary condition was applied to the fastener to establish the initial clamping force. The inertia of the piston assembly and the truncated portion of the connecting rod was represented by a point mass $M = 480\,\mathrm{g}$ coupled to the cut face. The value of M is lower than the equivalent mass m_{eq} used in the analytical model because the mass and inertial response of the retained lower part of the connecting rod are represented directly by the finite element bodies and their assigned density.

Determining N_{crit} by manually solving a separate model for every candidate engine speed would be cumbersome and computationally inefficient. Instead, the preload is established once in the first load step, and the rotational-speed ramp is applied progressively to the solution substeps of the second load step. The analysis remains static: the Ansys time parameter is used only as a load-progression variable, not as physical time. A MAPDL command snippet defines a table relating pseudo-time to the acceleration corresponding to the RPM sweep, allowing the contact state to be evaluated continuously as the inertial load increases.

MAPDL load definition and RPM sweep

```
R   = 40.259
L   = 147.10
K   = R/L
PI  = 3.14159265

! RPM sweep from RPM_min to RPM_max
RPM_min = ARG1
RPM_max = ARG2
T0 = 1.0        ! end of preload step
T1 = 2.0        ! end of RPM ramp
NPTS = 300      ! table resolution

*DIM,ACEL_TAB,TABLE,NPTS,1,1,TIME

*DO,I,1,NPTS
    FRAC  = (I-1)/(NPTS-1)
    RPM_I = RPM_min + FRAC*(RPM_max-RPM_min)
    W_I   = RPM_I*PI/30
    A_I   = -R*(W_I**2)*(1+K)
    ACEL_TAB(I,0) = T0 + FRAC*(T1-T0)
    ACEL_TAB(I,1) = A_I
*ENDDO

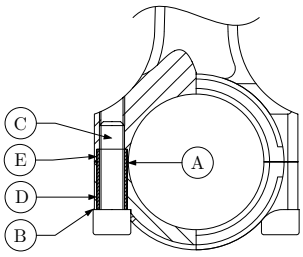
! ------------------------------
! Load Step 1: bolt pre-load
! ------------------------------
TIME,T0
ACEL,0,0,0
SOLVE

! ------------------------------
! Load Step 2: RPM ramp
! ------------------------------
TIME,T1
ACEL,0,0,%ACEL_TAB%
KBC,0
NSUBST,50,300,50
AUTOTS,ON
OUTRES,ALL,ALL
SOLVE
```

2.5 Contacts

Five contact regions were defined to represent load transfer between the individual components.

	Contact	Target	Type
A	Cap face	Rod face	Frictional, $\mu = 0.2$
B	Cap	Screw head	Frictional, $\mu = 0.2$
C	Rod thread	Engaged screw	Bonded
D	Cap	Dowel	Frictional, $\mu = 0.2$
E	Rod	Dowel	Bonded



Joint separation was assessed using a Contact Tool applied to contact region **A**. Two complementary indicators were monitored at every solution substep: the minimum contact pressure and the contact status on the rod–cap interface. As the inertial load increases, the contact status can progress from sticking to sliding while the mating faces remain in contact. The onset of separation is identified when the minimum contact pressure first reaches zero and the corresponding part of the interface changes to the near-contact state, indicating that the faces have opened but remain within the contact-detection range. The associated pseudo-time is then converted into the critical engine speed N_{crit}.

3 Results

3.1 Finite Element Results

Automatic time stepping reduces the pseudo-time increment near separation, improving nonlinear contact convergence and providing sufficient RPM resolution to identify the critical speed. Minimum contact pressure is the primary separation criterion, with gap and status used as secondary confirmation.

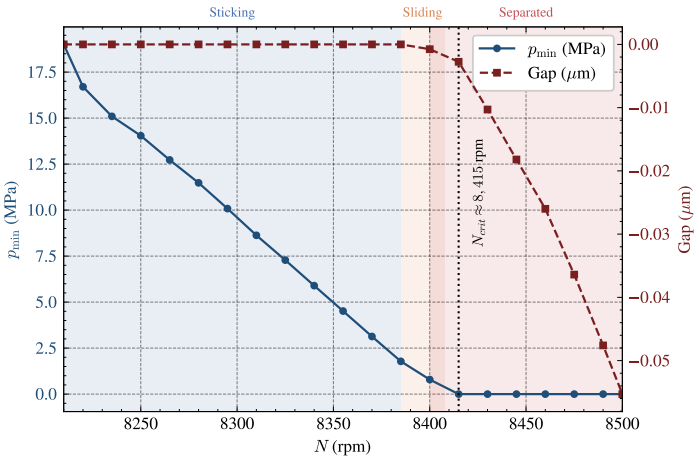
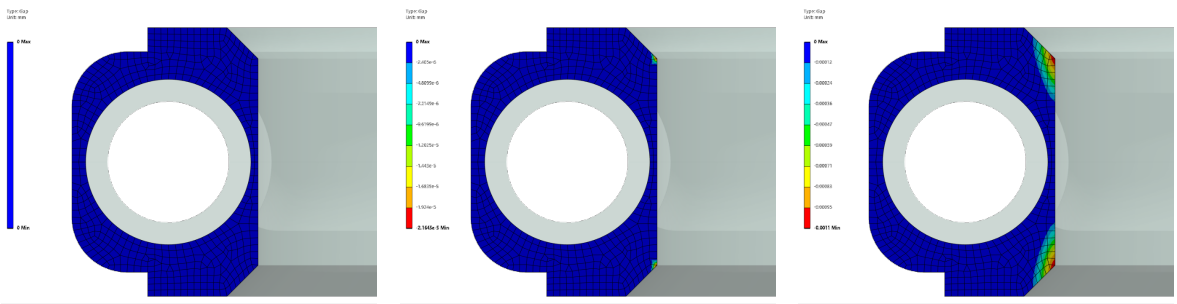


Figure 2: The shaded regions indicate the contact-status transition from sticking to sliding and separation.

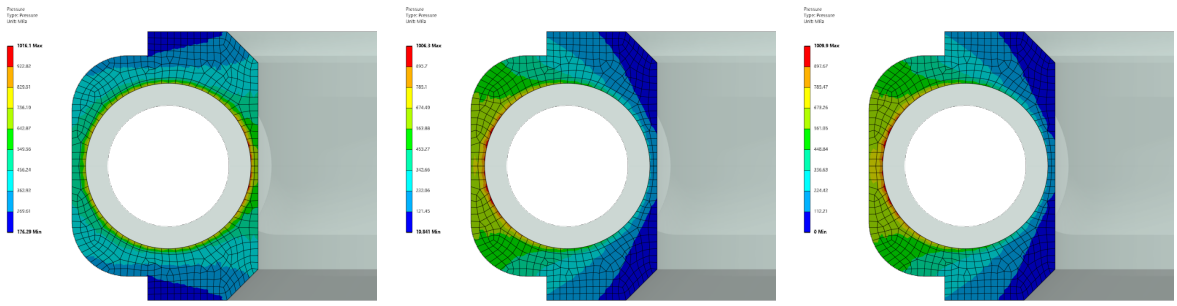
The resulting critical speed is therefore

$$N_{\text{crit,FEM}} \simeq 8415\,\text{rpm}.$$



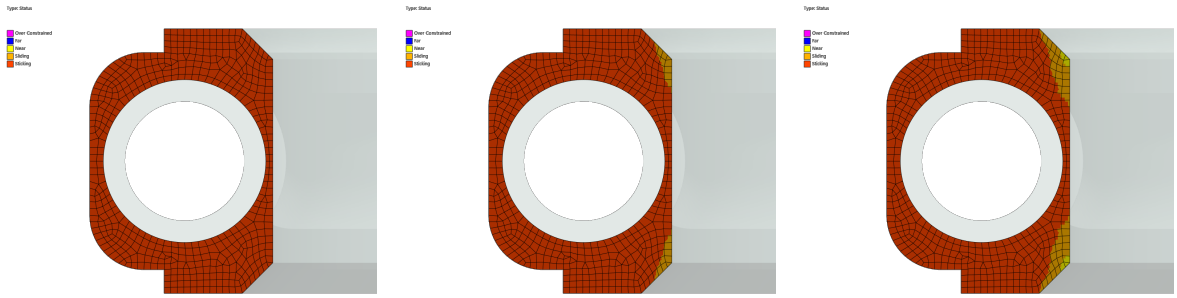
(a) After preload. (b) At gapping. (c) Separation

Figure 3: Gap (mm)



(a) After preload. (b) Before opening. (c) At gapping.

Figure 4: Contact-pressure (MPa)



(a) After preload (sticking) (b) Before opening (sliding) (c) At gapping (near)

Figure 5: Contact-status evolution from sticking to sliding to near at separation.

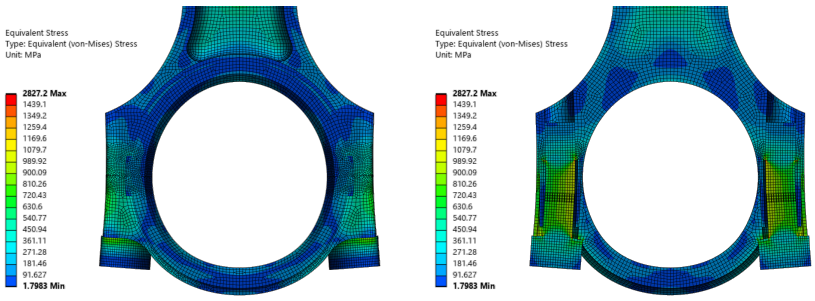


Figure 6: σ_{id}^{vM} (MPa)

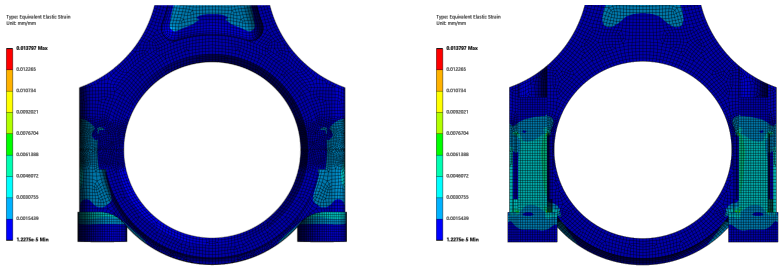


Figure 7: ε_{id}^{vM}

4 Discussion of Results

4.1 Comparison with Theoretical or Empirical Predictions

The FEM prediction is close to the analytical value of $N_{\text{crit,an}} \simeq 8770\,\text{rpm}$. Taking the analytical result as the reference, the percentage difference is

$$\Delta N_{\%} = \frac{|N_{\text{crit,FEM}} - N_{\text{crit,an}}|}{N_{\text{crit,an}}} \cdot 100 = \frac{|8415 - 8770|}{8770} \cdot 100 \simeq 4.05\%.$$

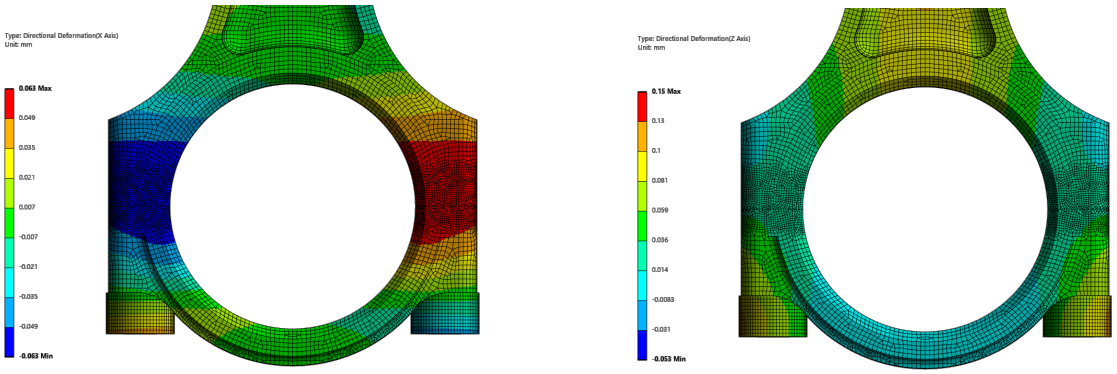
This close agreement supports the analytical representation of the joint.

4.2 Influence of Modelling Assumptions

The maximum deformation along the direction defining the eccentricity is $\delta_x^{\max} = 0.06\,\text{mm}$. Therefore,

$$\Delta e < \delta_x^{\max} = 0.06\,\text{mm} \ll e = 33.5\,\text{mm},$$

which validates the assumption that e remains approximately constant during loading.



(a) $\xrightarrow{x}$ (b) $z \uparrow$

Figure 8: Directional deformation at the onset of gapping (mm).

The FEM results also support the analytical assumption that the hollow dowel pin can be neglected in the pull-out equilibrium. The average shear stress in the dowel is approximately $\tau_{\text{avg}} = 1\,\text{MPa}$ and its effective shear-transfer area is $A_{\text{dowel}} = 754\,\text{mm}^2$. The corresponding resultant shear force is therefore

$$T = \tau_{\text{avg}} A_{\text{dowel}} \simeq 754\,\text{N} = 0.754\,\text{kN}.$$

This force is only about 2.9% of the analytical inertial load at the predicted critical speed ($F_{\text{inr}} \simeq 25.9\,\text{kN}$). Its contribution to resisting rod–cap separation is therefore small, supporting its omission from the analytical model.

4.3 Mesh Independence Study

A global mesh-independence study was performed using element sizes of 150%, 100%, 80% and 60% of the baseline size. For each mesh, the RPM ramp was solved through the separation region, since evaluating only a single load point at the nominal critical speed would not reliably identify the onset of gapping. The 150% mesh overpredicted N_{crit}, whereas the result stabilised from the 100% mesh onwards. The variations between the three finest meshes were smaller than the RPM sampling resolution of the load ramp, indicating mesh independence within the resolution of the analysis.

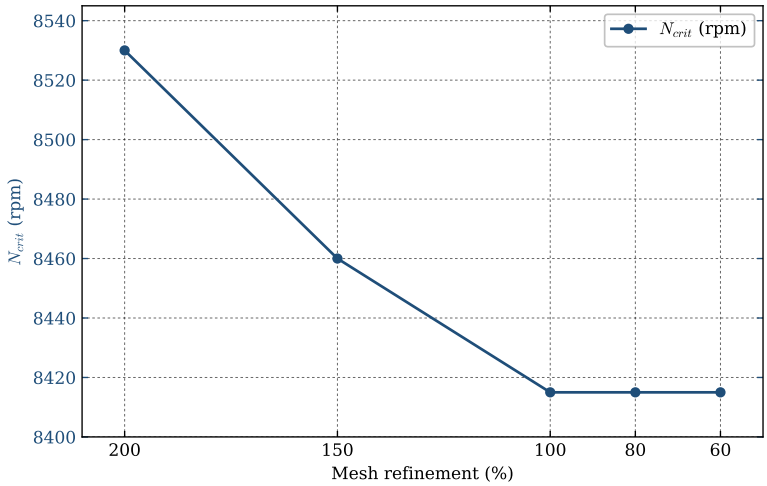


Figure 9: Critical engine speed as a function of global mesh refinement.

The model is intended to predict deformation and contact opening rather than detailed local stresses. Elevated stresses occur at sharp corners where fillets were omitted to limit the mesh count; these local artefacts are therefore excluded as assessment criteria. The convergence of N_{crit} in the mesh-independence study supports the separation predictions despite these localised stress peaks.

4.4 Model Limitations and Possible Improvements

The locating dowel pins of this type are generally installed with an interference fit, whereas this interference and its associated local contact pressure were omitted from the both in the FEM and in the analytical model. Future work could include, more detailed thread and bearing representations, and the full time-dependent engine cycle. The influence of the simplified crankpin support could be assessed by varying the angle of the constrained bore arc. A more detailed model could instead include the crankshaft geometry and contact between the crankpin and the big-end bore. Nevertheless, the close agreement between the analytical and FEM results indicates that the present model captures the dominant mechanism governing joint separation.